CANCER THERAPY

MEDDOCS
— International —

Nano-Drug Delivery System of Design and Struture for Cervical Cancer Photothermal Therapy

Xuwu Zhang; Dawei Gao*

State Key Laboratory of Metastable Materials Science and Technology, Applying Chemistry Key Lab of Hebei Province, Yanshan University, No.438 Hebei Street, Qinhuangdao, 066004, China.

Corresponding Author: Dawei Gao

State Key Laboratory of Metastable Materials Science and Technology, Applying Chemistry Key Lab of Hebei Province, Yanshan University, No.438 Hebei Street, Qinhuangdao, 066004, China.

Email: dwgao@ysu.edu.cn

Introduction

As a malignant disease, cancer causes a large number of deaths worldwide every year due to its high morbidity and high fatality rate. According to the global cancer statistics report provided by the World Health Organization (WHO), there were 18.1 million new cancer cases and 9.6 million deaths worldwide in 2018. In 91 of the 172 countries around the world, cancer has surpassed cardiovascular and cerebrovascular diseases and become the leading cause of human death [1]. Among them, cervical cancer is a serious one, with nearly five hundred thousand women developing the disease each year worldwide. Most women with early-stage tumor can be cured, although long-term morbidity from treatment is common. Results of randomised clinical trials have shown that for women with locally advanced cancers, chemoradiotherapy is regarded as the standard of care; however, the applicability of this treatment to women in less developed countries remains largely untested. Many women with localized tumor even now receive various combinations of surgery and radiotherapy, despite unresolved concern about the morbidity of this approach compared with definitive radiotherapy or radical surgery. Treatment of recurrent cervical cancer remains largely ineffective.

Therefore, the search for effective diagnosis and treatment methods is a critical problem to be solved urgently in front of scientific researchers from all over the world. At present, the most common clinical cancer treatment is still surgical resection of tumor lesions, and on this basis, adjuvant chemotherapy and radiation therapy. However, this treatment method has the

following defects: First, surgical resection often removes large areas of tumor lesions and surrounding normal tissues to avoid residual cancer cells. This method not only causes great damage to the normal body, but also cannot completely avoid metastasis and recurrence of cancer cells; secondly, chemotherapy and radiation therapy are systemic and local indifferent treatment methods, respectively, which have a strong killing effect on cancer cells and normal cells, severely destroying the body's immune system, causes different levels of permanent damage to various tissues and organs. During chemotherapy and radiation therapy, patients often experience symptoms such as hair loss, vomiting, bleeding, infection, and abnormal hematopoietic function. Therefore, the search for new treatment methods to achieve effective treatment of cancer and minimize the toxic and side effects on the normal body has become an urgent issue in the field of cancer treatment.

Nano-drug Delivery System (NDDS) is a kind of nanoparticles composed of high molecular substances, which can carry chemotherapy drugs and efficiently deliver drug molecules to the lesion. Its size is between 1-1000 nm, and its morphology can be designed and synthesized according to factors such as synthetic materials, functional properties, and local physiological characteristics of the lesion, such as capsule, sphere, rod, star, core-shell structure, etc. In recent years, there has been an increasing number of research reports on the nano-drug delivery system in the field of cancer treatment, which is mainly due to the unique advantages of the NDDS, such as improved pharmacokinetics, enhanced drug accumulation in tumor tissues, and reduced drugs on normal tissue side effects, etc. According to the literature, since the early 1950s, many types of drug delivery systems have been developed and applied to cancer treatment [2]. Through experiments on different animal models and patients, it has been proved that the drug delivery system can effectively improve the drug delivery efficiency and enhance the therapeutic effect of the drug. Among them, some drug delivery systems have entered clinical trials.

All along, the main goal of the tumor treatment process is to maximize the therapeutic effect of the drug itself, such as chemotherapy drugs, radioisotopes and targeted preparations, etc., so as to effectively kill the tumor cells; at the same time, it is to treat normal cells and the toxic and side effects of tissues are minimized [3,4]. In the past few decades, various NDDSs including microspheres, liposomes, proteins, polymers and nanoparticles have been designed and successfully synthesized, and a series of animal and clinical trials have been carried out to test their therapeutic effect [2,3]. Although there are differences in drug delivery methods and drug delivery routes between different drug delivery systems, the ultimate goal is the same, that is, to achieve targeted drug delivery of tumor tissue. By changing the pharmacokinetics and pharmacodynamics [5], the drug delivery system extends the circulation time of the drug in the body, increases the concentration and retention time of the drug at the tumor tissue, improves the solubility of the hydrophobic drug, and enhances the ease of degrading the stability of the drug, while reducing the drug's immunogenicity and systemic toxicity.

However, with further research, many drug carriers have not shown good therapeutic effects on patients, especially for the treatment of malignant tumors [6]. Compared with traditional methods, the therapeutic effect is not significantly improved,

and some unexpected toxic and side effects occur. Many drug delivery systems have failed in clinical trials at different stages. For example, many conjugates of chemotherapy drugs and polymers, including doxorubicin, camptothecin, paclitaxel, etc [7-9], have failed in clinical trials and have not been approved for clinical treatment. The reason is that although the application of the drug carrier has increased its accumulation in tumor tissue compared with chemotherapy alone, the study found that the results of drug accumulation in human experiments are different from those obtained in animal experiments. In addition, there are many significant individual differences between different patients, that is, the amount of drug accumulation in the tumor tissue of different patients is different [8]. Therefore, how to reduce the individual differences between patients, realize the specific drug release of the drug carrier in the tumor tissue, and effectively increase the amount of drug accumulation is a major challenge in the field of drug carriers.

Photothermal Therapy (PTT) provides answers to the above questions. PTT is a promising anti-tumor strategy due to inherent advantages of minimum invasiveness, high spatiotemporal selectivity and easy operation [10,11]. On the one hand, by constructing a light-responsive nano drug-loading system, the responsive release of drugs can be achieved. On the other hand, hyperthermia can cause cell membrane disruption, protein and DNA degeneration and vessel occlusion, resulting in direct and irreversible damage to tumor cells and tissues [12-14]. Light source and photothermal agents are two essential elements for PTT. NIR light with the range of 700-900 nm can penetrate 10cm in biological soft tissues and therefore is widely used for phototherapy and medical imaging [15-17]. Currently, many types of photoactive nanomaterials, including organic pigments (e.g., melanin, light-absorbing polymer), semiconductor, graphene and noble metal (e.g., gold, silver) have been explored as photothermal agents [18,19]. Although great successes have been obtained in these studies, there remain several fundamental problems and technical obstacles. Organic components are usually confronted with low photothermal conversion efficiency and severe photobleaching [20]. It is well-established that in organic nanomaterials are promising candidates for photothermal agents due to great molar extinction coefficient, high light-to-heat conversion and tumor selective accumulation [21,22]. Unfortunately, inorganic substances inevitably meet a puzzle, that is potential cytotoxicity, which usually requires surface modifications or polymer envelopment to settle [23,24]. Therefore, exploitation of photothermal agents with features of strong NIR-responsiveness, high energy conversion efficiency and photostability, and good biocompatibility is desperately needed for the advance of a biomedical platform.

In our study, we have successfully synthesized many different nano drug delivery systems for tumor PTT, such as gold based drug delivery systems (gold nanoshell coated liposome [25], branched gold nanoshell coated liposome [26]), polydopamine/gold-nanorod composite drug delivery system [27], peptide-directed silver nanocages [28] and graphene oxide based drug delivery system [29]. They all displayed excellent photothermal effect and inhibitory effect for HeLa/U14 cells in *vitro/vivo*.

Gold based drug delivery systems for PTT

Gold nanoparticles coated liposomes and their anti-tumor efficacy
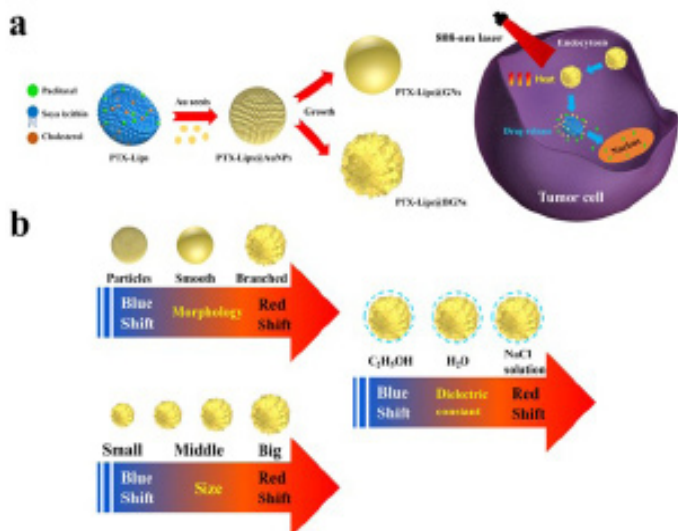
Scheme 1: (a) Schematic Illustration of the Synthesis Route for the PTX-Lips, PTX-Lips@AuNPs, PTX-Lips@GNs, and PTXLips@BGNs and the NIR Laser Irradiation-Induced Chemo-Photothermal Therapy in Tumor Cells; **(b)** Regulation of LSPR Absorption with Various Morphologies, Sizes, and Dielectric Constants of Surrounding Mediums [26].

Gold nanoparticles have attracted tremendous efforts cancer therapy and bioimaging on account of inherent attributes such as biocompatibility, stability, tunable optical properties. However, the lack of LSPR absorption in the NIR region limits their application in PTT. Hence, over the past decade, some promising strategies under clinic investigation have focus on various kinds of NIR-sensitive gold nanomaterials via using gold nanoparticles as seeds. These gold nanomaterials have a remarkable red shift of LSPR absorption in the NIR region at the side of gold nanoparticles. The main influential factors of the red shift to NIR region are morphology, size and dielectric constant of surrounding medium. In other words, for one kind of gold nanomaterial, we can tune the location of LSPR absorption peak to NIR to some extent via regulating its morphology, size and dielectric constant of surrounding medium. Directly, the photothermal effect of gold nanomaterials will be enhanced under the NIR laser irradiation, which affects the drug release of PTT-agent-combined drug delivery nano-systems and anti-tumor efficacy. Nevertheless, to the best of our knowledge, although numerous preparations of gold nanomaterials have been illustrated, the regulatory mechanism of these nanomaterials is still not fully understood. How the morphology, size and dielectric constant of surrounding medium influence their LSPR absorption has been the issue we aim to solve.

To this end, we present a drug delivery system based on gold nanomaterials coated liposomes with various morphologies (gold nanoparticles, gold nanoshells [25] and branched gold nanoshells [26]), sizes and dielectric constant of surrounding mediums. The photothermal effect of gold nanomaterials drives the phase transformation of liposomes to release drug under the NIR laser irradiation, which evolves synergistic cancer therapy by deep thermal ablation and chemotherapy (**Scheme 1**) [26]. Furthermore, we studied the mechanism of red shift based on gold nanoparticles to form gold nanoshells and branched gold nanoshells, which regulates the LSPR absorption to NIR region.

Synthesis of gold based liposomes

At first, paclitaxel, soya lecithin and cholesterol were mixed into ethanol as the lipid phase. Tween-80 and PEG-2000 were solubilized in phosphate-buffered saline as the aqueous phase. Then, the lipid phase was added drop wise into the aqueous phase under magnetic stirring for 2 hours. In this approach, liposomes with nanoscale were prepared. Reduced L-Glutathione (GSH) was added drop wise into the prepared liposomes, and then the mixture solution was stirred gently for 2 hours. Gold seeds were synthesized by the chemical reduction of $AuCl_3$ solution with $NaBH_4$. Both the $AuCl_3$ solution and the freshly prepared $NaBH_4$ solution were put into an ice bath for 4 min and protected from light. Afterward, ice-cold $NaBH_4$ was immediately added to the $AuCl_3$ solution. After vigorous stirring, Au seeds formed promptly and were transferred to room temperature within 30 min. Finally, gold seeds were put into the prepared liposomes. The resulting solution was gently mixed in a shaking incubator and then stored for 20 hours. The gold nanoparticles coated liposomes (Au NPs-Lips) were formed.

Based on above, we synthesized two different systems: Gold Nanoshell coated liposome (GNS) and Branched Gold Nanoshell coated liposome (BGNS). (1) $AuCl_3$ solution was added to the Au NPs-Lips, followed by the addition of $NaBH_4$. After 4 h of stirring at room temperature, $AuCl_3$ and $NaBH_4$ solution were added to the resulting mixture and allowed to react for 4 h under ambient conditions. The GSN were obtained. (2) $AuCl_3$ solution was added to the Au NPs-Lips, followed by the addition of $HONH_3Cl$. After 4 h of stirring at room temperature, $AuCl_3$ and $HONH_3Cl$ solution were added to the resulting mixture and allowed to react for 4 h under ambient conditions. The BGNS were prepared.

Characterization of gold based liposomes

In order to confirm the morphologies, Au NPs-Lips, GNS and BGNS were analyzed by TEM (**Figure 1 a-d**). The liposomes were coated by Au seeds with different concentrations. As outlined in TEM images, gold seeds uniformly adhered to the surface of the liposomes. Following the gold nanoparticles growing, GNS and BGNS were obtained via using various reductants. Remarkably, the surface of BGNS was more branched than GNS. The UV-vis-NIR absorption spectrum confirmed the effect of morphology on LSPR absorption (**Figure 1e**). Less Au nanoparticles-based liposomes showed the similar properties of gold nanoparticles (520 nm). As the gold nanoparticles gathering on the liposomes, a slight red shift of LSPR absorption peak was exist, which centered at about 550 nm. In the wake of adding the $AuCl_3$ solution and reductant, gold nanoparticles were grown on the liposomes sequentially to form GNS, which was found to exhibit a broad LSPR absorption peak centered at 580 nm. The surface of GNS became branched to be BGNS while the kind of reductant and the time of reduction were changed and therewith the LSPR absorption peak showed red shift to about 630 nm. Above UV-vis-NIR absorption spectrum confirmed the effect of morphologies to LSPR absorption of these nanomaterials. The photothermal performance of these nanomaterials was suggested as well. As shown in **Figure 1f**, the Au NPs-Lips showed a low temperature rise with 808-nm laser irradiation compared with GNS and BGNS owing to the lack of LSPR absorption in NIR region. After 10 min irradiation with 808-nm laser at 2.0 W/cm², the temperatures of GNS and BGNS solution increased from 27⁰C to 57⁰C and 27⁰C

to 68°C, respectively, which indicated that tuning the LSPR absorption to or near to NIR region enhanced the photothermal performance of these nanomaterials. As nanoliposomes, temperature rise leads to the phase transformation, which releases the drug controllably. The release profiles of paclitaxel from Au NPs-Lips, GNS and BGNS were outlined in **Figure 1g**. The drug release depends on the temperature, which illustrates that BGNS showed higher level of drug release.

Figure 1: Effect of morphology to LSPR of gold-based drug carriers. **(a-d)** TEM images of less and more gold nanoparticles-coated PTX-Lips, PTX-Lips@GNS and PTX-Lips@BGNs. **(e)** UV-vis-NIR absorption spectra and **(f)** Photothermal profile with 808 nm laser of less and more gold nanoparticles-coated PTX-Lips, PTX-Lips@GNs and PTX-Lips@BGNs at the same concentration. **(g)** Light-responsive drug release and **(h)** Cell viability of HeLa cells treated with PTX-Lips@AuNPs, PTX-Lips@GNs and PTX-Lips@BGNs under 808 nm laser irradiation [26].

Inhibitory effect for HeLa cells in *vitro*

To investigate the anti-tumor efficacy, the possible cytotoxicity of Au NPs-Lips, GNS and BGNS towards HeLa cells is probed (**Figure 1h**).The relative viability of the Hela cells incubated with Au NPs-Lips, GNS and BGNS for 24 h was determined by the MTT assay. For one kind of nanomaterial, the anti-tumor efficacy enhanced with the increase of paclitaxel. Besides, for the same concentration of paclitaxel, the BGNS showed much better effect of photothermal therapy. These results demonstrated the distinctive LSPR absorption and much better chemo-thermal anti-tumor efficacy treated with BGNS compared with Au NPs-Lips and GNS.

Regulatory mechanism of photothermal

The regulatory mechanism was investigated likewise. First, the Au NPs-Lips with less gold nanoparticles showed the properties of gold nanoparticles alone, which were found to exhibit a LSPR absorption peak at about 520 nm. Next, a red shift to about 550 nm was happened with the increase of the concentration of gold nanoparticles.

According to Rayleigh scattering formula:

$$S = \frac{32\pi^2 R^3 m (n^2 - 1)^2}{\lambda^4 (n^2 + 2)^2}$$

(S: Scattering coefficient, R: Radius, n: Refractive index, m: Concentration of nanoparticles), the scattering coefficient of long wave is smaller than that of short wave. Thus, the scattering of short wave is stronger than long wave for nanoparticles. With the concentration of gold nanoparticles increased, the

numbers of scattering times was increased as well. As a result, the red shift of LSPR absorption peak was occurred. Finally, after further growing, the sizes of gold nanoparticles became much bigger and irregular to form GNS and BGNS, whose LSPR absorption peaks centered at about 580 and 630 nm. On the basis of the surface electron density theory of metal nanoparticles:

$$\lambda_m{}^2 = \frac{c^2 m \pi}{N_e e^2}(\varepsilon_0 + 2n_0{}^2)$$

(λ_m: Absorption peak of nanoparticles, c: Concentration of metal, m: Effective mass of electron, N_e: Free electron density on metal surface, e: Electron charge, ε_0: High frequency dielectric constant of metal, n_0: Refractive index of solvent). Compared with the GNS, superficial area of the BGNS was bigger due to its branched surface, which leaded to the smaller free electron density on the surface of gold nanoshells. Therefore, BGNS was found to exhibit red shift of LSPR absorption at the side of GNS.

So as to investigate the effect between size and LSPR absorption, BGNS with various sizes were analyzed by TEM and DLS (**Figure 2 a-d**). As a result, the BGNS, which synsesized through disparate amount of $AuCl_3$ solution and reductant,were about 90, 110, 130 and 150 nm respectively. Note that the different sizes were of no effect on their morphologies. With the increase of the size of BGNS, the UV-vis-NIR showed a slight red shift (**Figure 2e**) and the photothermal performance was enhanced accordingly (**Figure 2f**). On account of the different photothermal performance, the BGNS with higher temperature exhibited much better drug release (**Figure 2g**). For researching the anti-tumor efficacy, the possible cytotoxicity of BGNS with various sizes towards Hela cells is also explored. As shown in **Figure 2h**, the BGNS with big size illustrated much better anti-tumor efficacy. These results confirmed the BGNS showed red shift of LSPR absorption peak and enhanced anti-tumor efficacy with the increase of the size.
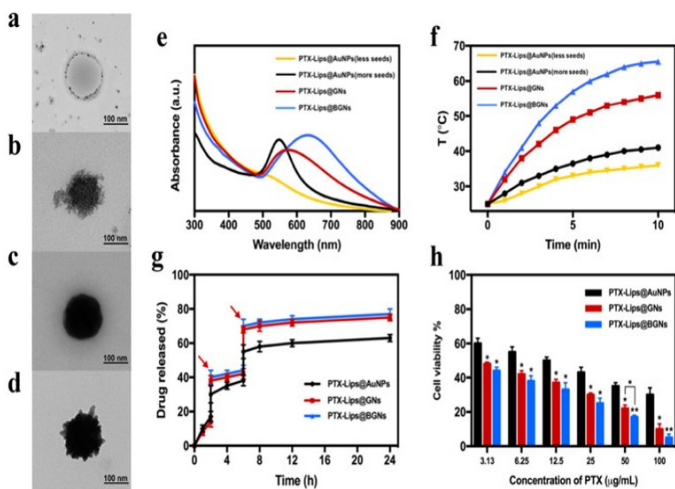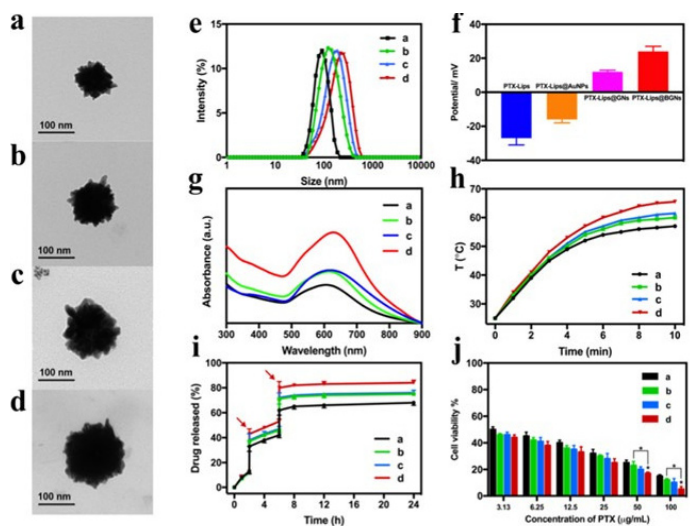

Figure 2: **(a-d)** TEM images of BGNS with increscent sizes. **(e)** DLS size analysis, **(g)** UV-vis-NIR absorption spectra, **(h)** photothermal profile with 808 nm laser, **(i)** Light-responsive drug release and **(j)** Cell viability of HeLa cells treated with BGNS with increscent sizes and the same concentration under 808-nm laser irradiation (a, b, c, d are corresponding to size-increased BGNS in TEM images). **(f)** Zeta potential of PTX-Lips, AuNPs, GNS and BGNS [26].

Once made into nanoscale, the materials show different properties compared with macroscale. The BGNS with various sizes followed the quantum size effect. Kudo proposed a relation between energy level spacing and particle diameter:

$$\delta = \frac{4E_f}{3N} \propto \frac{1}{V} \propto \frac{1}{d^3}$$

(E_f: Fermi level, N: Electron number of one nanoparticle, V: Volume, d: Arrange particle size). The energy level spacing becomes short with the increase of particle size. Hence, the transition energy of electron is little, which leads to the LSPR absorption peak of BGNS red shift. From perspective of surface effect, atoms are located on the surface of the nanoparticles with decrease of size. Thus, the specific surface area and relative number of atoms on the surface increase. Adjacent atoms around the surface atoms are missing, which causes insufficient coordination of the atoms due to the dangling bonds. The surface atoms have higher activity. Delocalized electrons reallocate between surface and interior, which leads to the increase of bond strength and chemical bond force constant. Therewith, the blue shift is occurred.
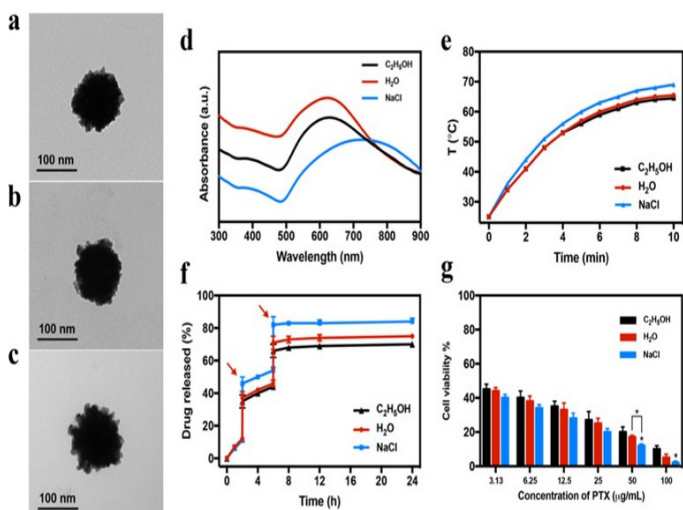
Dielectric constant of surrounding medium

Figure 3: (a-c) TEM images of BGNS in C_2H_5OH, H_2O and NaCl solution. **(d)** UV-vis-NIR absorption spectra, **(e)** Photothermal profiles with 808 nm laser, **(f)** Light-responsive drug release and **(g)** Cell viability of HeLa cells treated with BGNS in C_2H_5OH, H_2O and NaCl solution at the same concentration under 808-nm laser irradiation [26].

Given that the dielectric constant of surrounding medium affects the LSPR absorption of nanomaterials, we investigated LSPR absorption and anti-tumor efficacy of BGNS in C_2H_5OH, H_2O and NaCl solution. As shown in **Figure 3 a-c**, TEM images showed that there was no significant distinction, which indicated that the surrounding mediums do not affect the morphology and construction of BGNS. Compared with C_2H_5OH and H_2O, NaCl solution group exhibited a remarkable red-shift broad peak centered at about 750 nm (**Figure 3d**). The UV-vis-NIR absorption spectra confirmed the effects of dielectric constant of surrounding medium to regulate the LSPR absorption of BGNS to NIR region. Due to the LSPR absorption peak was in the NIR region, NaCl solution group exhibited superior photothermal performance, drug release and anti-tumor efficacy under 808-nm laser irradiation (**Figure 3 e-g**).

According to the relation between the LSPR frequency and dielectric constant of surrounding mediums:

$$\omega_p^2 = \frac{ne^2}{\varepsilon m_{eff}}$$

(ω_p: LSPR frequency of metal, n: Electron density, ε: Dielectric constant of surrounding medium, m_{eff}: Effective mass of electron). The LSPR frequency decreases with the increase of the dielectric constant of surrounding medium

$$\omega_{NaClsolution} > \omega_{H_2O} > \omega_{C_2H_5OH}, \text{ so}, \omega_{NaClsolution} < \omega_{H_2O} < \omega_{C_2H_5OH}$$

Therefore, remarkably, NaCl solution group showed red shift of LSPR absorption peak compared with H_2O and C_2H_5OH groups.

NIR light triggered size variable drug delivery system

The novel nanoplatform namedPDA@GNRs-DOX/Ce6for drug delivery and PTT was designed and synthesized, in which anti-tumor drug DOX modified Gold Nano Rods (GNRs) and Chlorine6 (Ce6) were loaded on the surface of Polydopamine (PDA) nanospheres (**Scheme 2**) [27]. The synthesized nanomedicine could accumulate primarily in the tumor sites through EPR effect, then the system converted the light to heat accompanying the PDA nanospheres degradation and separation of GNRs from the multifunctional nanocomplexes under the irradiation of NIR laser. At the same time, DOX was also released from GNRs in tumor microenvironment with laser irradiation for chemotherapy, and Ce6 produced $^1O_2$ for photodynamic therapy after being irradiated with 660 nm laser. Furtherly, the dissociative gold nanorods penetrated into the interior of tumor to realize deep PTT. Our study showed the cluster bomb structures combined with DOX and Ce6 can kill HeLa cells almost entirely.
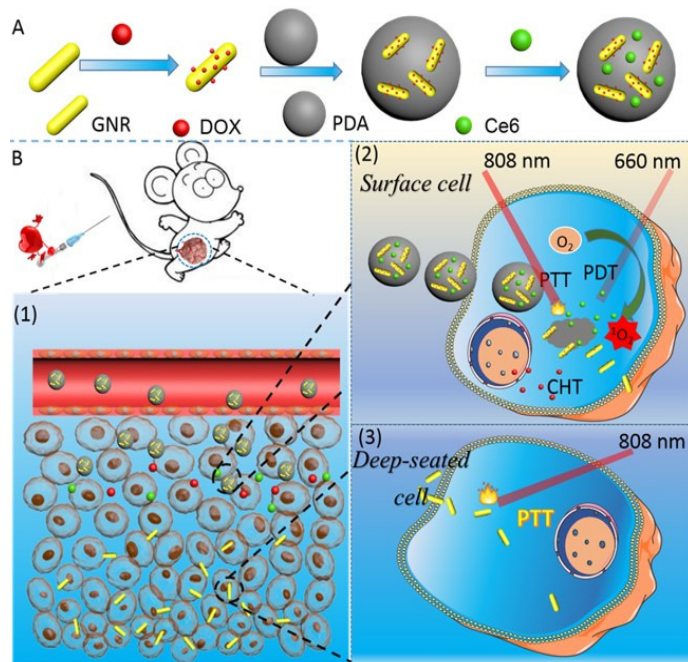
Scheme 2: Schematic illustration of PDA@GNRs-DOX/Ce6 synthesis and mechanism for treating tumors. **(A)** Synthesis of PDA@GNRs-DOX/Ce6. **(B)** (1) Release of DOX, Ce6, and GNRsfrom nanoplatform and their distribution into deep tumor under laser irradiation. (2) PDA@GNRs-DOX/Ce6 mediated chemotherapy and phototherapy in the superficial tumor cells after internalization. (3) GNRs penetrating into tumor parenchyma and accomplishing light-triggered photothermal ablation of the deep-seated malignant cells [27].

Synthesis ofPDA@ GNRs-DOX/Ce6

Gold nanorods were prepared by a seed growth method [30]. In a typical synthesis method, Cetyltrimethylammonium Bromide (CTAB) solution was mixed with $HAuCl_4$ aqueous solution with continuous stirring. Ice-cold $NaBH_4$ was added into the solution, the color of solution changed to brownish yellow, so the seed solution was obtained. To prepare the growth solution, CTAB aqueous solution was add into $AgNO_3$ at 25 °C, then $HAuCl_4$ and HCl were added into the above mixture, and ascorbic acid was added after gentle mixing to yield colorless growth solution. Finally, the seed solution was added to the above prepared growth solution at 30-33 °C for 12 h. The color of the solution gradually changed to red. The excessive CTAB was removed by repeated centrifugation twice, the supernatant was discarded and the GNRs was re-suspended with Milli-Q water. Then, 0.05 mL of PEG-2000was added into 9.75 mL of GNRs aqueous solution and the mixture was vigorously stirred for 24 h. DOX aqueous solution was added into the mixture followed by continuous stirring for 24 h. The solution was centrifuged twice, and the precipitate was dispersed in Milli-Q water to prepare successfully the GNR-DOX.

The synthesis of PDA nanospheres was carried out in the alkaline solution. Firstly, dopamine was added to Tris-buffer solution (pH 8.5) stirring for 1 h. The mixture was centrifuged at 8000 rpm, and then the obtained supernatant was centrifuged at 14000 rpm and washed with Milli-Q water for three times. Finally, the collected precipitate was dissolved in 1mL of Milli-Q water. The prepared PDA was incubated with gold nanorods (modifying DOX) for 10 min and then centrifuged at 8000 rpm to remove the non-bound PDA and gold nanorods. Ce6 solution was added into the mixture for 24 h. Then, the mixture was centrifuged at 8000 rpm and washed for three times with water. The precipitate was dissolved in 1mL of water, the PDA@GNRs-DOX/Ce6 were prepared successfully.

Characterization of PDA@ GNRs-DOX/Ce6

Homogeneous and dispersed GNRs with length of 48 nm and width of 15 nm were prepared (**Figure 4A**). On this basic, to introduce chemotherapy into this system. PEG-2000 was used to modify the nanostructure surface before loading DOX to generate GNRs-DOX. After PEG-2000 modification, the zeta potential of GNRs decreased from 28.6 ± 0.4 mV to −3.7 ± 0.2 mV, which resulted in the further loading doxorubicin by electrostatic binding. The zeta potential of GNR@DOX increased to 11.3 ± 0.6 mV (**Figure 4C**), which could be attributed to the DOX on the GNRs surface. TEM images showed that there was no significant morphology difference between GNRs-DOX and GNRs (**Figure 1**B).
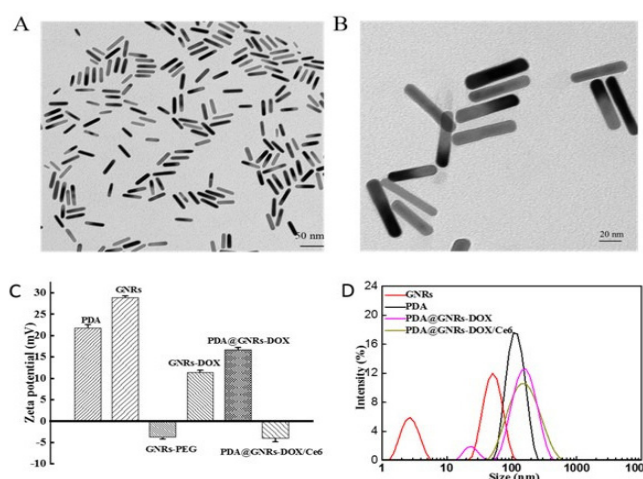
Figure 4: (A-B) TEM images of GNRs, GNRs-DOX. **(C)** Zeta potentials of PDA, GNRs, GNRs-PEG, GNRs-DOX and PDA@ GNRs-DOX/Ce6. **(D)** Sizes distributions of GNRs, PDA, PDA@GNRs-DOX and PDA@GNRs-DOX/Ce6 [27].

PDA is easy to integrate with GNRs-DOX, because PDA possess a strong adhesion feature [31,32]. The uniform PDA nanospheres exhibited average size of 125.8 ± 0.4 nm. (**Figure 4**D, **5**A). The images of the PDA@ GNRs-DOX/Ce6 nanoparticles indicated their uniform morphology (**Figure 5**B). The average size of PDA@GNRs-DOX/Ce6 increased to 169.6 ± 0.6 nm. The above results indicated the successful synthesis of PDA@GNRs-DOX/Ce6 nanoparticles. The research found that the size between 100 and 200 nm was acknowledged as the best particle size for EPR effect, which is the main mechanism for passive targeting of nanoparticles to tumor site [33-35].The presence of C, N, O and Au elements in PDA@GNRs-DOX/Ce6 was confirmed by energy dispersive spectroscopy (EDS) (**Figure 5**C). The successful synthesis of PDA@GNRs-DOX/Ce6 was further affirmed by X-ray photoelectron spectroscopy (XPS) (**Figure 5**D).
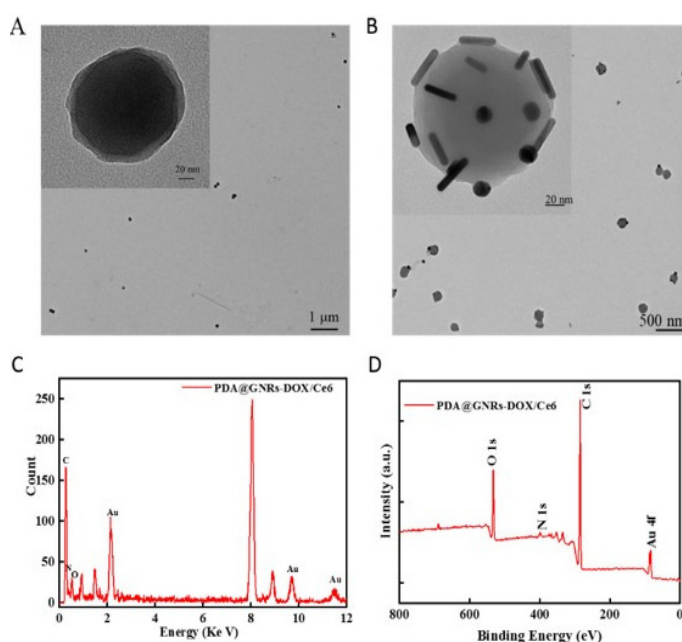
Figure 5: (A-B) TEM images of PDA and PDA@GNRs-DOX/Ce6. **(C)** EDS of PDA@GNRs-DOX/Ce6. **(D)** XPS broad survey spectrum of PDA@GNRs-DOX/Ce6 [27].

Photothermal effectof PDA@ GNRs-DOX/Ce6

Moderate hyperthermia (41 - 43 °C) was an effective method for killing the tumors, which had little harm to normal cells because tumor cells were more sensitive to high temperature than normal cells [36-38]. To reveal the photothermal performance of the PDA@GNRs-DOX/Ce6, photothermal conversion capability was investigated. The infrared photothermal images of PDA@GNRs-DOX/Ce6 solution at the concentration of 96.8 $\mu g\ mL^{-1}$ were recorded under 808 nm laser irradiation (1.5 W cm^{-2}) for 5 min. (**Figure 6**A). The temperature of PDA@GNRs-DOX/Ce6 exposed to NIR showed a rapid elevation to 54.8 °C within 5 min (**Figure 6**B). Next, the light-responsive structural change of PDA@GNRs-DOX/Ce6 was evaluated by TEM and size distribution. Initially, the average diameter of PDA@GNRs-DOX/Ce6 significantly increased to 440 nm, which was morphology change with the resultant aggregation or fusion with an 808 nm

NIR laser at 1.5 W cm⁻² for 1 cycle (turn on-off 5 min laser, respectively). Subsequently, average diameter of the nanomedicine decreased to 150 nm after 2 cycles of irradiation and finally changed to 50 nm extending laser irradiation (3 cycles). Separation of GNRs from PDA@GNRs-DOX/Ce6 under laser irradiation could be observed by TEM (**Figure 6 C,D**) and this result was consistent with that of size distribution. These results indicated that GNRs were successfully detached from the carriers under 808 nm laser irradiation, which raises the possibility of deep penetration tumor sites. Above these results attributed to that the nanocarriers can convert the light to heat, accompanying with the PDA nanospheres photo degradation and separation of GNRs from the multifunctional nanocomplexes under 808 nm lasers. Therefore, the separated GNRs still possess excellent photothermal ability, which could penetrate into the interior tumor tissue to damage the tumor stem cells in the deep site.
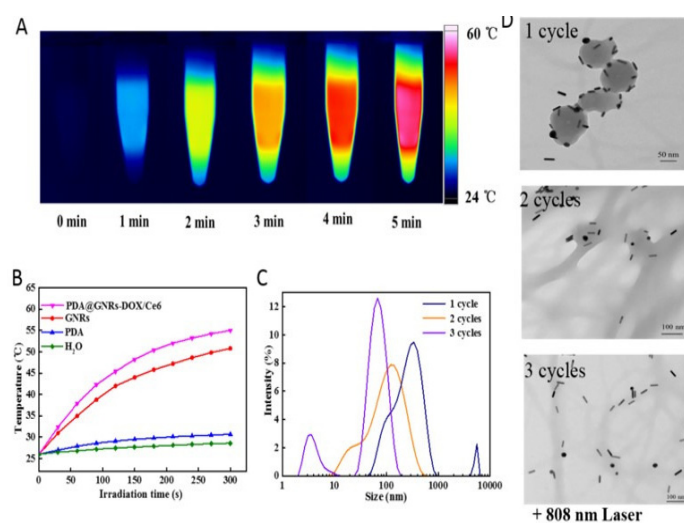

Figure 6: (A) Photothermal images of PDA@GNRs-DOX/Ce6 solution exposed to NIR at regular intervals. **(B)** Temperature elevation profiles of GNRs and PDA@GNRs-DOX/Ce6 solutions with laser irradiation at 808 nm; water and PDA were used as blank and negative controls, respectively. **(C)** Size variation of PDA@GNRs-DOX/Ce6 solution for different cycles upon laser irradiation. **(D)** TEM images of PDA@GNRs-DOX/Ce6 solution exposed to NIR at regular intervals [27].

Inhibitory effect for HeLa cells in *vitro*

MTT assay was carried out to evaluate the biocompatibility of PDA@GNRs-DOX/Ce6. There were 46.72 %, 58.23 %, 70.50 % and 69.30 % of survival cells in the free DOX, GNRs-DOX, PDA@GNRs-DOX, PDA@GNRs-DOX/Ce6 treated groups, respectively. Among the groups, the free DOX exhibited the highest toxicity at the same concentration (**Figure 7**A). The low toxicity of PDA@GNRs-DOX and PDA@GNRs-DOX/Ce6 could be attributed to both stable structures formed by DOX and GNRs, which delayed DOX leakage. The HeLa cell viability was 20.09 ± 2.50 % through photothermal therapy combining with chemotherapy of PDA@GNRs-DOX/Ce6, and the cell survival rate was only 14.75 ± 1.30 % under 660 nm laser irradiation (**Figure 7**B). The fluorescence live/dead cells staining were also investigated. As shown in **Figure 7**C, in the DOX, Ce6, or GNRs alone-treated groups, the cells exhibited green fluorescence, which is consistent with the MTT results. For synergistic therapy, the green fluorescence was reduced to some extent in PDA@GNRs-DOX/Ce6 group (808 nm laser for 2 min). Importantly, almost all the cells treated PDA@GNRs-DOX/Ce6 (808 nm plus 660 nm laser for 2 min) were dead

in irradiated region, demonstrating the remarkable synergistic chemo-photothermal-photodynamic tumor therapy effects of PDA@GNRs-DOX/Ce6, which displayed a synergistic effect leading to obviously higher cytotoxicity than any single treatment pattern.

Biodistribution study in *vivo*

Kunming mice bearing U14 tumor were treated by PDA@GNRs-DOX/Ce6 to explore the tissue distribution of Au element. The major organs and tumor tissues were removed at different periods after the mice were intravenous injected with the PDA@GNRs-DOX/Ce6 (**Figure 8**A). The majority of PDA@GNRs-DOX/Ce6 accumulated in the tumor at 4 h after injection, and the content of Au element in the tumor sites was up to 9.6 µg/g. The results showed the excellent tumor accumulation of nanomedicine by EPR. Additionally, the Au element was also found in liver and spleen at 4 h and then cleared from the body after 7 days, indicating that gold element could be effectively cleared from body. These results indicated that PDA@GNRs-DOX/Ce6 were biosafety.

Penetration tumor tissues and therapeutic effect for U14 tumor in *vivo*

Owing to the strong tissue penetrability of NIR [39], real-time thermal imaging in *vivo* was taken by a photothermal camera to visualize the photothermal conversion of nanomedicine (**Figure 8**B). The results showed that the temperature of PDA@GNRs and PDA treatment (1.5 W cm⁻², 2 min) were higher than that of GNRs (1.5 W cm⁻², 4 min) with the same Au/PDA concentration. The possible reason is that single small size of GNRs were not easy to accumulate at tumor site. Furthermore, the content of Au in *vivo* was evaluated to verify this hypothesis (**Figure 8**C). The results indicated that it was difficult for small size of nanoparticles (GNRs) to reach and further accumulate in tumor site by EPR effect compared with large size of nanoparticles (PDA and PDA@GNRs). Therefore, GNRs plus laser was impossible to achieve the high therapeutic effect in *vivo* compared with in *vitro*.

According to the result of **Figure 8**B, the temperature of tumor-surrounding was much lower than that of tumor region, so only tumor cells can be thermally damaged while normal cells avoided the damage. Temperature of tumor zone exposed to laser rose rapidly and reached about 51.2 °C. The relative tumor volume (V/V₀) in the PDA@GNRs group was 6.50 ± 2.56, which was obviously lower than that of PDA group under NIR irradiation (**Figure 8**D, E), which may be attributed to the disintegration and penetration into tumor of PDA@GNRs. These results indicated that PDA@GNRs possess excellent accumulated into the tumor sites by EPR effect, then the system converted the light to heat accompanying the PDA nanospheres degradation and separation of GNRs from the multifunctional nano complexes under the irradiation of NIR laser. The dissociative gold nanorods penetrated into the interior of tumor to realize deep PTT.

Under NIR laser irradiation, the DOX, GNRs and Ce6, just like a variety of bombs, were released from PDA@GNRs-DOX/Ce6, which exhibited the synergy effect of photothermal, chemo and photodynamic therapy at the superficial sites of tumor tissues. Subsequently, the released GNRs could penetrated into the interior tumor tissue to damage the tumor stem cells. Therefore, this type of nano-drug with light stimulation response was promising to provide a feasible approach for tumor therapy by nano-drug penetrating into tumor cells deeply.
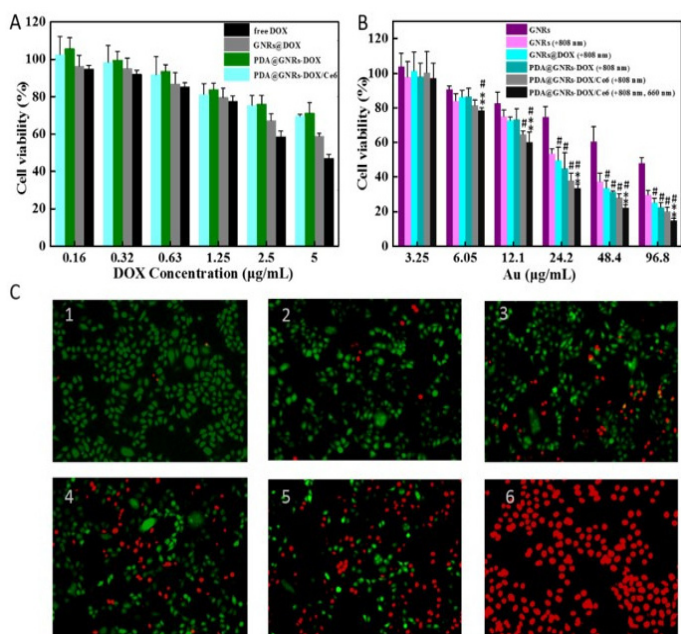
Figure 7: Cytotoxicity of HeLa cells treated with different formulations. **(A-B)** Relative viability of HeLa cells after 24 h of incubation with different concentrations of DOX or Au. **(C)** Fluorescence images of HeLa cells incubated with PBS with 660 nm laser 240 mW cm^{-2} and 808 nm laser 1.5 W cm^{-2}(1), Ce6 with 660 nm laser 240 mW cm^{-2} (2), DOX (3), GNRs plus 808 nm laser 1.5 W cm^{-2}(4), PDA@GNRs-DOX/Ce6 plus 808 nm laser 1.5 W cm^{-2}(5), PDA@GNRs-DOX/Ce6 plus 660 nm laser 240 mW cm^{-2} and 808 nm laser 1.5 W cm^{-2}(6) [27].
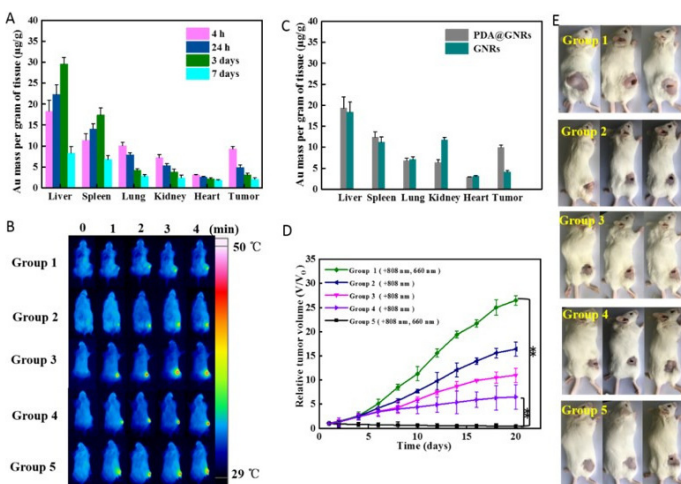

Figure 8: (A) Biodistribution of Au in *vivo* after intravenous injection. **(B)** Biodistribution of Au after intravenous injection of PDA@GNRs and GNRs at 4 h. **(C)** Infrared thermal images of tumor-bearing mice treated with different formulations. **(D)** Relative tumor volume of the treated mice after different treatments. **(E)** Digital photos of tumor bearing mice with different treatment at the 20th day. (Group 1: PBS 1.5 W cm^{-2} 808 nm laser irradiation and 240 mW cm^{-2} 660nm laser irradiation, Group 2: GNRs at the Au concentration 96.8 μg mL^{-1} under 1.5 W cm^{-2} 808 nm laser irradiation, Group 3: PDA 10 mg mL^{-1} under 1.5 W cm^{-2} 808 nm laser irradiation, Group 4: GNRs 96.8 μg mL^{-1} 2 W cm^{-2} 808 nm laser irradiation, Group 5: PDA@GNRs-DOX/Ce6 1.5 W cm^{-2} 808 nm and 240 mW cm^{-2} 660 nm laser irradiation) [27].

Peptide-directed silver nanocages for PTT

Biomineralization is a green, simple, and precise way in synthesis of organic-inorganic hybrid [40-42]. Proteins are widely participating in biomineralization (e.g., ferritin [43]) *via* mediating nucleation and growth. Inspired by natural phenomena, peptides are becoming popular to the bottom-up synthesis of the inorganic components for their tailored structural modularity and accompanying molecular recognition and programmable self-assembled structure [44,45]. Also, peptides can selectively combine with the crystal plane of metal NPs to control their size and crystal form [46,47]. Peptide-based hybrids are widely used as functional materials with a feature of high spatial precision and tunable physicochemical performance [48,49]. Peptides have been used as structure-defined scaffolds to control the synthesis various inorganic nanomaterials (e.g., Ag, Au, Pd NPs) to work as antibacterial, catalyst, imaging agent and signal sensing probe [50-54]. However, to the best of our knowledge, the peptide-mineralized metal architecture capable of ultra strong plasma response has not been reported. It is possible to rationally control the architectural organization of plasmonic metal by designing the structure of peptides and regulating the process of corresponding mineralizing. Octreotide (OCT) has been proved to be a template to mediate the growth of inorganic substance, because it possesses multiple coordination sites (e.g., amino, hydroxy and imidazole groups) to strongly bind metal surface and control their growth [55-57]. Meanwhile, OCT shows good biocompatibility and long half-life period, and has been used as the targeting bullet to anchor cancer cells [58].

In this work, we described a structure controllable Ag NCs, which can be facilely prepared by a biomineralization method and applied to high efficiency PTT [28]. Ag NCs exhibit a remarkably enhanced surface plasmon response and display NIR absorption up to 900nm, because of the hollow nanoshell structure with strongly coupled Ag NPs. We systematically investigate the growth kinetics of the control factors, including the duration of incubation and the dosage of AgNO$_3$, which have significant effects on the size and morphology of the Ag NCs, resulting in tunable optical properties. In addition, Ag NCs are endowed with superior photothermal performance, including high light-to-heat conversion efficiency and excellent photostability under 808nm laser irradiation..

Preparation of Ag NCs

To synthesize Ag NCs, AgNO$_3$was used as the precursor, NaBH$_4$ and ascorbic acid (H$_2$Asc) were used as strong and mild reducing agents, respectively, and OCT was used as a peptide template, where substoichiometric amount of NaBH$_4$ was added to the mixed solution of precursor, peptide and ascorbic acid. In a typical process, AgNO$_3$(3.4 mM)was first incubated with OCT (0.25 mM) and H$_2$Asc (7 mg mL^{-1})for 24 h followed by addition of NaBH$_4$ (15 mM). It has been reported that amine or carbonyl groups can chelate Ag and control the growth of Ag nanoparticles [59-62]. In the experiment, OCT not only combined with AgCl to control the crystal growth and structures, but also chelated silver ions on their outer surface. After addition of sodium borohydride, the Ag$^+$ of AgCl@OCT/Ag$^+$ was reduced to Ag^0 and attached to the surface of complexes to form Ag seeds. The AgCl nanocubes were then reduced to metallic silver to the surface of the seeds and gradually dissolved [63,64], eventually forming hollow cage (**Scheme 3**).
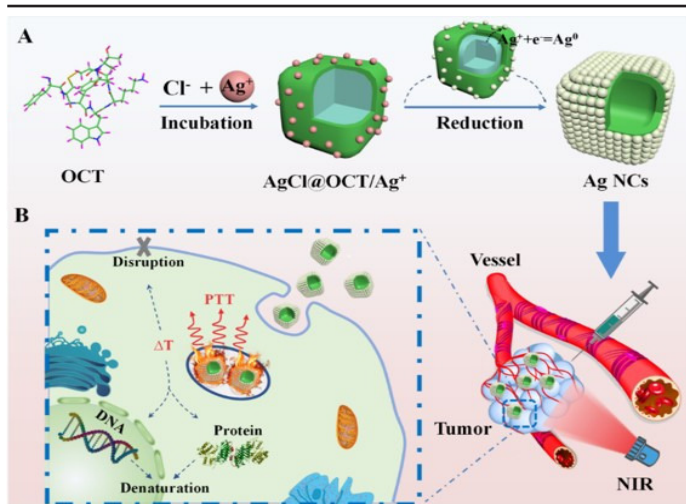
Scheme 3: Schematic illustration of the synthesis of Ag NCs using OCT as the biotemplate and their application as a PTA against tumor [28].

Photothermal effects of Ag NCs

The photothermal conversion capabilities of the Ag NCs are investigated. Under 808 nm laser (1.5 W cm⁻²) irradiation for 5 min, the temperature of Ag NCs shows a rapid elevation to 65.8°C during the irradiation process (**Figure 9a**). In contrast, the temperature of Ag NPs and ultrapure water are only increased to 30.8 °C and 24.7 °C under the same conditions, respectively. The photothermal conversion characteristic of Ag NCs can be better visualized by real-time thermal imaging (**Figure 9b**).

Photothermal stability is an important element of photothermal agent because photodegradation can greatly limit the effect of photothermal ablation. We evaluate the photostability of Ag NCs by repeated irradiation the solution using NIR laser at 1.5 W cm⁻² for 5 min. The temperature elevation for Ag NCs does not decay significantly during 10 cycles of irradiation (**Figure 9c**). In addition, the UV-vis absorption spectrum and the morphology of Ag NCs have negligible change after 0.5 h of irradiation (**Figure 9d**). The excellent photothermal stability of Ag NCs suggests that the intermolecular interactions of peptide and Ag NPs are strong enough to resist the disturbance from increase of temperature. At the same time, the saline solutions of Ag NCs were stored at 4 °C for one month. The storage stability of Ag NCs was analyzed by comparing the UV-vis spectra of different storage time. After storage for two weeks and a month, the absorption intensity of the solutions at 808 nm can still reach 95% and 92% compare to the initial absorbance, respectively, so the Ag NCs have good long-term storage stability. As the temperature above 46 °C can cause cells to undergo direct tissue necrosis, coagulation, and carbonization [65,66], the Ag NCs can be served as an excellent photothermal reagent.

The photothermal transduction efficiency of the Ag NCs is calculated [67]. Ag NCs were irradiated with an 808 nm laser with an energy power density of 1.5 W cm⁻² until reaching equilibrium, then the laser was switched off, and the suspension was naturally cooled to ambient temperature. During the cooling stage, the change of temperature with time is monitored

(**Figure 9e**), which is fit to a linearized energy balance to measure the light-to-heat conversation efficiency (η) of Ag NCs (**Figure 9f**). The value of η for the Ag NCs is calculated to be 46.1%, significantly higher than that of Au nanorods (22%) [68].
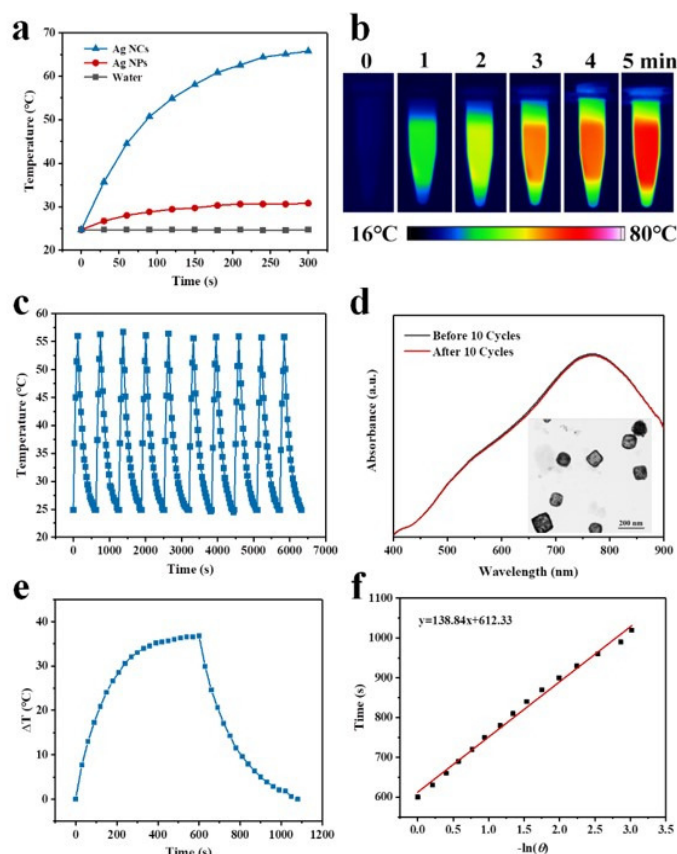

Figure 9: **(a)** Temperature elevation profiles of Ag NPs and Ag NCs solutions at the same concentration under laser irradiation, water was used as the negative control. **(b)** Photothermal images of the Ag NCs solution at different time intervals irradiated. **(c)** Temperature variation of the Ag NCs solution for ten on/off cycles upon laser irradiation. **(d)** UV-vis spectra of Ag NCs before and after the irradiation. Inset is TEM image after laser irradiation for 0.5 h. **(e)** The photothermal response of the aqueous dispersion of Ag NCs for 600 s with an NIR laser and then the laser was shut off. **(f)** Linear time data versus $-\ln\vartheta$. Unless otherwise noted, the concentration of Ag NCs was 48 μg mL⁻¹, and an 808nm laser was used at power density of 1.5 W cm⁻² [28].

In *Vitro* cytotoxicity and photothermal therapy for HeLa cells

The Ag NCs can efficiently and sustainably convert the NIR light energy into substantial amounts of thermal energy, implying that they have great potential as a photothermal agent for PTT. Before in *vivo* tests, the biosafety of the Ag NCs is evaluated on HeLa and 293T cells by using MTT assay. The Ag NCs do not exhibit significant cytotoxicity for two kinds of cells at the concentration of 6-60 μg mL⁻¹ without laser treatment (**Figure 10a,b**). In contrast, pure Ag NPs are more toxic to both types of cells than Ag NCs. It is reported that silver toxicity mainly originates from dose-dependent silver ions [69,70]. The enhanced cytocompatibility for Ag NCs may because that the peptide template can act as an electron-hole scavenger to avoiding silver ion formation [71-73].
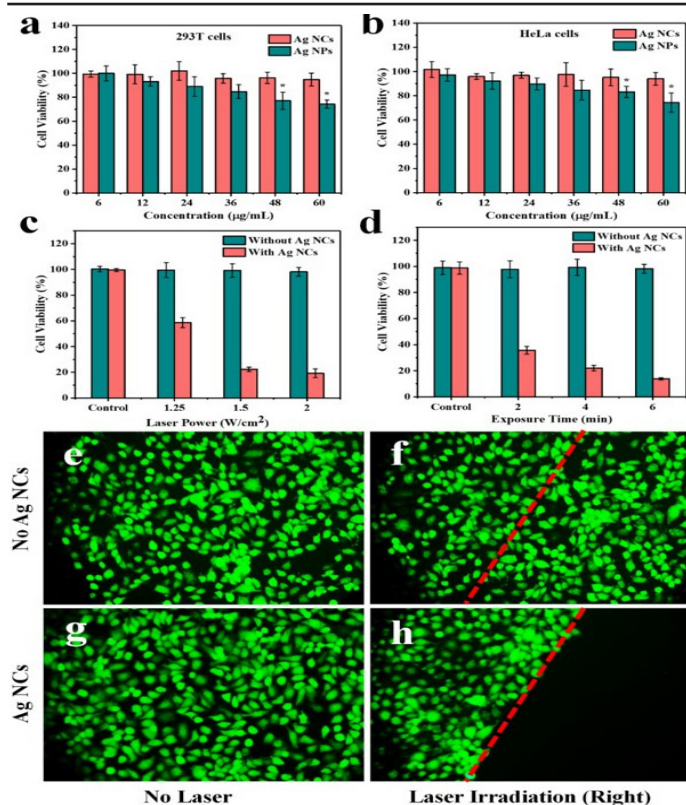
Figure 10: Cell viabilities of **(a)** 293T cells and **(b)** HeLa cells after incubation with different concentrations of Ag NPs and Ag NCs. Viabilities of HeLa cell incubated with 48 μg mL^{-1} of Ag NCs at **(c)** Different power densities and **(d)** Different durations of 808nm laser irradiation. Fluorescence images of live stained HeLa cells incubated without **(e, f)** and with **(g, h)** The Ag NCs (48 μg mL^{-1}). Cells were irradiated by 808nm laser at power densities of 1.5 W cm^{-2} for 5 min [28].

The photothermal therapy effect in *vitro* is evaluated by HeLa cells, which is subjected to 808 nm laser illumination in the presence and absence of Ag NCs. After the incubation with 48 μg mL^{-1} of Ag NCs, HeLa cells are illuminated for 5 min the resulting cell viability decrease significantly as the laser intensity increase from 1.25 to 2 W cm^{-2} (**Figure 10c**). The cell viabilities of HeLa cells decrease dramatically as the increase of irradiation time at 48 μg mL^{-1} of Ag NCs and 1.5 W cm^{-2} illuminations (**Figure 10d**).

To visually evaluate the PTT effect, fluorescent live/dead cell staining experiments are performed. Cells treated with either Ag NCs or laser alone emit green fluorescence due to being stained with FDA (**Figure 10 e-g**), which is indicative of their live state. This fluorescence in the exposed area disappears where cells are pre-incubated with Ag NCs, resulting in a clear demarcation line for died and live cells (**Figure 10h**), which further confirms the antitumor efficiency of Ag NCs in the PTT.

In *Vivo* Photothermal Ablation for U14 Tumor

To verify the in *vivo* photothermal effect caused by Ag NCs, the temperature changes in *vivo* were monitored by a thermal imaging camera. It is clear that the temperature of the irradiation area in the mice treated with Ag NCs is higher than that in the mice treat with saline at all the time points (**Figure 11 a**). For the mice injected with Ag NCs, the tumor temperature rises rapidly and reached up to a plateau of ~52.2 °C (**Figure 11b**), which is sufficient to kill cancer cells through thermal ablation and restrict their malignant proliferation. In the case of mice injected with saline solution, the tumor temperature only slight

increased by ~3 °C, which demonstrates that the promising potential of Ag NCs as an excellent photothermal agent.

To shed more light on the photothermal ablating effect of Ag NCs, the relative tumor volume in different groups of mice were monitored every 2 days after the treatment. The tumors on mice treated with Ag NCs after NIR irradiation shows greatly inhibited growth curve (V/V$_0$=0.44 ± 0.24) and are nearly ablated after 14 days treatment(**Figure 11c**), resulting in a tumor growth inhibition value (82.688 ± 4.32 %) is significantly higher than that of control groups (**Figure 11d**).
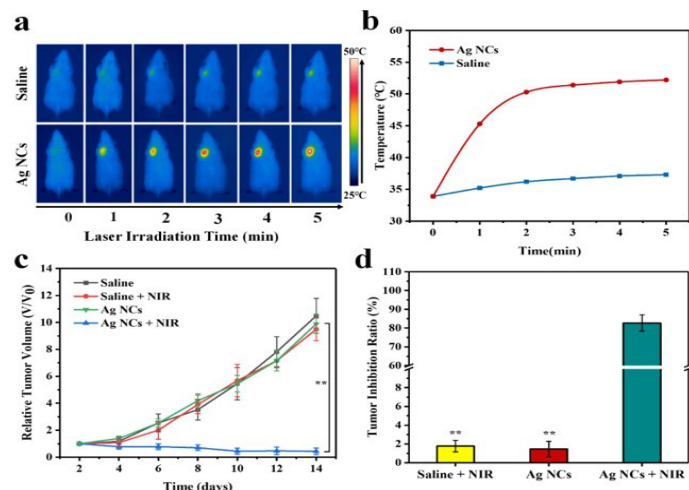

Figure 11: (a) *In vivo* thermal images of mice injected with saline or the Ag NCs under NIR laser irradiation. **(b)** Tumor temperature profiles as the function of laser irradiation time. **(c)** Growth curves of tumors in different groups of mice after treatment. **(d)** The tumor inhibition ratio of different groups of mice [28].

Drug delivery system based on graphene oxide for PTT

Graphene oxide, as a typical representative of two-dimensional carbon material, has been extensively applied in drug carriers for the following reasons. First, GO is nontoxic at certain concentration levels and biodegradable (85 μg/mL *in vitro* and 10 mg/kg *in vivo*) [74,75]. Moreover, GO contains hydrophilic functional groups, endowing its chemical functionalization and water-solubility. GO has a high specific surface area with many functional groups, such as hydroxyl (-OH) and epoxide (-O$^-$) groups in the basal plane and carboxylic acid (-COOH) groups at the edges [76,77]. These functional groups of GO can interact with electronegative atoms of drug molecules through hydrogen bonding. The ionizable carboxylic acid group at the edge of GO allows electrostatic interactions with drug molecules. Despite the presence of these functional groups, the basal plane of GO is mainly composed of polyaromatic networks, which allow drug molecules to bind through π-π stacking and hydrophobic interactions [78]. Therefore, GO could be connected with chemotherapy drugs or other therapeutic agents for synergistic therapy.

ICG, a NIR dye approved by the U.S. Food and Drug Administration (FDA) [79,80], has been intensively studied for PDT and PTT due to its NIR light optical features for biomedical applications [81,82]. NIR light in the range of 700–1100 nm, known as the optical tissue penetration window, can penetrate deeper into biological tissues than ultraviolet or visible light, so it is ideal for photo therapies including PDT and PTT [83]. In response to NIR laser irradiation, ICG at the ground singlet state can be activated to triplet state and then transfer its energy to triplet oxygen, further generate singlet oxygen [84], which can

cause cell death. Moreover, under NIR laser irradiation, ICG can convert the light energy into heat efficiently. Because the heat tolerance of tumor cells is lower than normal tissue [85], hyperthermia, introduced by ICG under NIR laser irradiation, is primarily to kill the tumor cells. However, along with the time of irradiation extending, the photothermal stability of ICG declines rapidly, which limits the application of ICG in PTT [86].

Herein, we developed a nanocomposite ICG-Wed-GO, through co-loading Wedelolactone (Wed) and ICG on the surface of GO by π–π stacking interaction (**Scheme 4**) [29]. As a natural antitumor drug, Wed is one of the active polyphenolic compounds extracted from *Wedelia calandulaceae* or *Eclipta prostrate* [87], which was proved to possess a wide range of antitumor properties through binding dsDNA, inhibiting to poisomerase IIα and blocking DNA synthesis [88]. By co-loading Wed and ICG on GO, ICG-Wed-GO could achieve the synergistic trimodal chemotherapeutic/PTT/PDT effects. Under 808 nm NIR irradiation, hyperthermia and ROS generated by ICG could effectively kill tumor cells. Meanwhile, heat will promote the Wed release and uptake by cells, which can further inhibit the tumor growth. Compared with traditional therapeutic strategies, ICG-Wed-GO is expected to be a more effective treatment for cancer therapy.
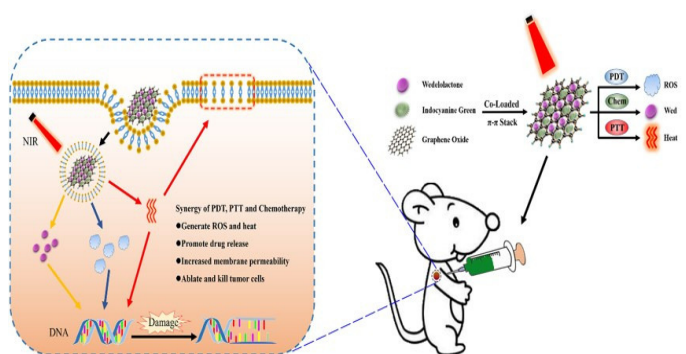
Scheme 4: Schematic illustration of the synergistic trimodal chemotherapeutic/PTT/PDT effects of ICG-Wed-GO [29].

Preparation of ICG-Wed-GO

In order to obtain nanoscale GO, GO powder was dispersed in ultrapure water and treated by ultrasonic probe under 600 W for 12 h in ice-water bath. Then, the GO solution was filtrated through 0.22 μm filter and stored in room temperature. Wed was dissolved in absolute ethyl alcohol, and Tween-80 was added to increase solubility. Then, Wed solution was mixed with the same volume GO solution under ultra sonication for 1 h. The mixture was continuously stirred by electric magnetic stirrer for 12 h. After that, absolute ethyl alcohol was removed completely by vacuum-rotary evaporation. The solution was centrifuged under 5000 rpm for 10 min to separate free Wed. Then, the Wedelolactone loaded Graphene Oxide (Wed-GO) was obtained. For the preparation of ICG and Wed co-loaded graphene oxide, ICG solution was mixed with the same volume Wed-GO and stirred for 12 h in the dark environment. In order to remove free ICG, the mixture was dialyzed in PBS for 24 h. The solution remained in dialysis bag was ICG-Wed-GO.

Characterization of ICG-Wed-GO

AFM imaging showed that the ICG-Wed-GO was lamellar with well dispersibility, and the thickness was 2-3 nm (**Figure**

12B, C). The average sizes of ICG-Wed-GO was 162.1 nm (**Figure 12D**). And the Zeta potentialswas -26.1 ± 1.5 mV (**Figure 12E**).After conjugating with Wed and ICG, the UV-Vis spectrum of ICG-Wed-GO showed two characteristic absorption peaks at 350 nm originated from Wed and at around 800 nm derived from ICG (**Figure 21F**), demonstrating the successful binding of Wed and ICG on GO. According to the concentrations of Wed and corresponding absorbance, we calculated the linear regression equation. As shown in **Figure 12G**, after diluting five times, the difference of absorbance value at 350 nm between GO and Wed-GO was 2.025. Through linear regression equation, the Wed loading efficiency was calculated (84.91 %).

Photothermal property in *vitro*

To investigate the NIR laser-induced PTT effect of ICG-Wed-GO, the samples were examined under continuous irradiation of 808 nm NIR (2 W/cm^2, 10 min). As shown in **Figure 13A** and **13B**, the real-time temperature changes of samples were recorded by temperature gauge and thermal imaging camera. After 10 min irradiation, the temperatures of ICG-Wed-GO reached 79.4 ^{0}C. Obviously, the ICG-Wed-GO exhibited more effective photothermal conversion property than other samples. It was observed that the temperature of free ICG first rose and then dropped, which confirmed the poor photothermal stability of free ICG. However, when conjugated GO with ICG, the photothermal stability of ICG improved remarkably. With the same concentration of ICG, the maximum temperature of ICG-Wed-GO in each cycle was much higher than that of free ICG (**Figure 13C**).The temperature of ICG-Wed-GO still reached up to 56 ^{0}C after 5 cycles, while the maximum temperature of ICG reached 41 ^{0}C. In addition, by combining the data of **Figure 13C**, the curve of photothermal stability was formulated (**Figure 13D**). After 5 cycles of 808 nm laser irradiation, the decrease of photothermal stability of free ICG and ICG-Wed-GO was 39.26 % and 29.56 %, respectively.
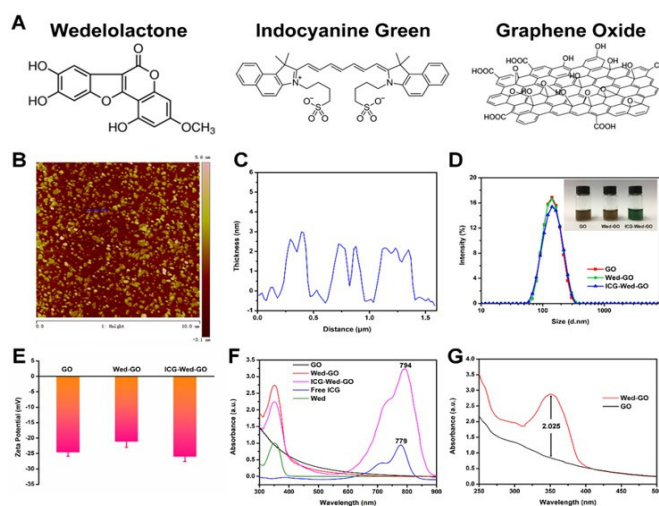

Figure 12: (A) Molecular structures of Wedelolactone, Indocyanine Green and Graphene Oxide. **(B)** and **(C)** AFM characterization of ICG-Wed-GO. **(D)** Size distribution of ICG-Wed-GO. The inset showed the photographs of GO, Wed-GO and ICG-Wed-GO. **(E)** Zeta potentials of GO, Wed-GO and ICG-Wed-GO. **(F)** UV-vis absorption spectra of GO, Wed-GO, Wed, Free ICG and ICG-Wed-GO. **(G)** UV-vis absorption spectra of GO and Wed-GO with the same GO concentration [29].
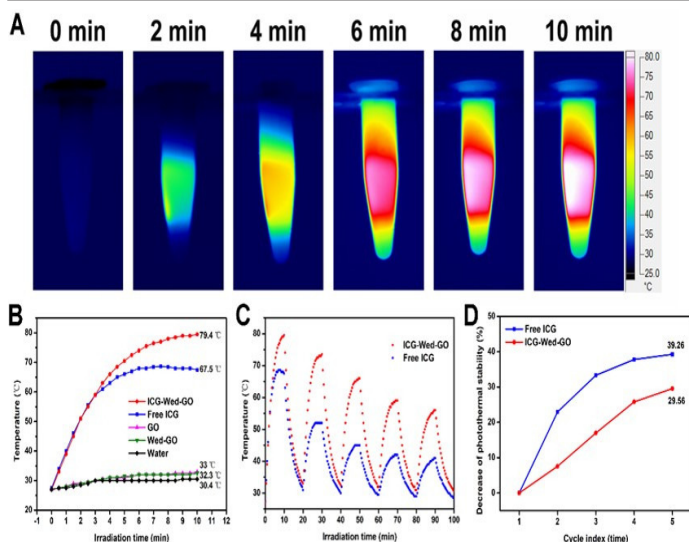
Figure 13: Photothermal and photodynamic effects of ICG-Wed-GO. **(A)** Thermal images of ICG-Wed-GO under laser irradiation for 10 min. **(B)** Photothermal curves of Water, Wed-GO, GO, Free ICG and ICG-Wed-GO. **(C)** Temperature evaluation of ICG-Wed-GO and Free ICG over five laser ON/OFF cycles. **(D)** Photothermal stability decrease curve of Free ICG and ICG-Wed-GO [29].

Inhibitory effect for HeLa cells in *vitro*

MTT assay was performed to evaluate the antitumor effect in*vitro*. HeLa cellswere treated by the samples with different concentration of Wed. Without the NIR irradiation (**Figure 14A**), there was no inhibition effect in GO group. The cell activities in Wed-GO and ICG-Wed-GO groups were reduced with the Wed concentration increased. At low Wed concentration, the inhibition effects in Wed-GO and ICG-Wed-GO groups were not obvious. When the Wed concentration increased to 40 µg/mL, the cell activities in Wed-GO and ICG-Wed-GO groups decreased to 61.92 % and 57.18 %, respectively. At the same time, under NIR laser treatment (2 W/cm^2, 1 min), the antitumor effect of ICG-

Wed-GO in*vitro* was improved significantly (**Figure 14B**). At the Wed concentration of 5 µg/mL, the cell activity in ICG-Wed-GO group with NIR irradiation was 48.83 %, which was lower than that without NIR irradiation at eight-fold of Wed concentration (40 µg/mL, 57.18 %). In **Figure 14C**, the ICG-Wed-GO with laser irradiation presented the best inhibition effect. Compared with other treatments, the cell activity inICG-Wed-GO with laser group was only 12.65 %.

Therapeutic effect for U14 tumor in *vivo*

To further examine antitumor effect in *vivo*, the tumor-bearing Kunming mice received an intratumoral injection of ICG-Wed-GO and were immediately exposed to an 808 nm laser with power density 2 W/cm^2 for 1 min. The temperature changes at the tumor site were monitored with an infrared thermal camera. The results showed that the tumor temperature increased rapidly with 808 nm laser irradiation (**Figure 15A**). After irradiation for 1 min, the tumor temperature reached up to 48 ^{0}C, which indicated the excellent photothermal property of ICG-Wed-GO in *vivo*.

In **Figure 15B** and **15C**, after 14-day treatment, the tumors in ICG-Wed-GO with NIR laser group were completely ablated. In addition, body weight changes were recorded during the treatment (**Figure 15D**), and no obvious weight change was detected. In the course of treatment, the tumor volumes were measured and calculated every other day (**Figure 15E**). After treated by ICG-Wed-GO with laser irradiation, the tumors of mice reduced gradually, and on the 10th day, the tumors disappeared completely. In contrast, only the ICG with laser irradiation group showed a certain suppressive effect, and the other treated groups did not show the obvious effect. After mice were sacrificed, the tumors were removed and weighed (**Figure 15F**). The trend of tumor weight was consistent with the results of tumor volume changes. Except the ICG-Wed-GO with laser irradiation group, the average tumor weight in ICG with laser group was 0.86 ± 0.16 g, which was lighter than those of other groups.
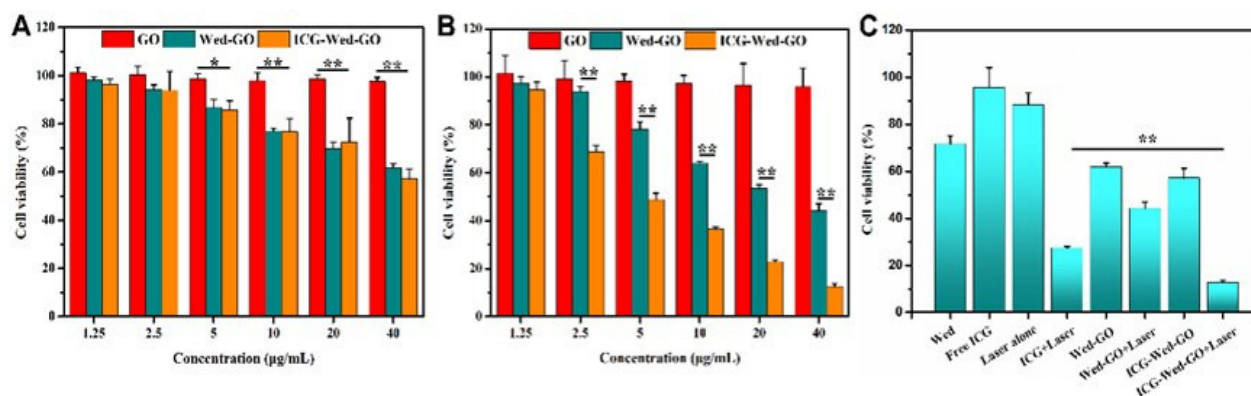

Figure 14: Relative viabilities of HeLa cells treated with various concentrations of GO, Wed-GO and ICG-Wed-GO without **(A)** and with **(B)** laser irradiation. **(C)** Relative viability of HeLa cells treated with different samples [29].
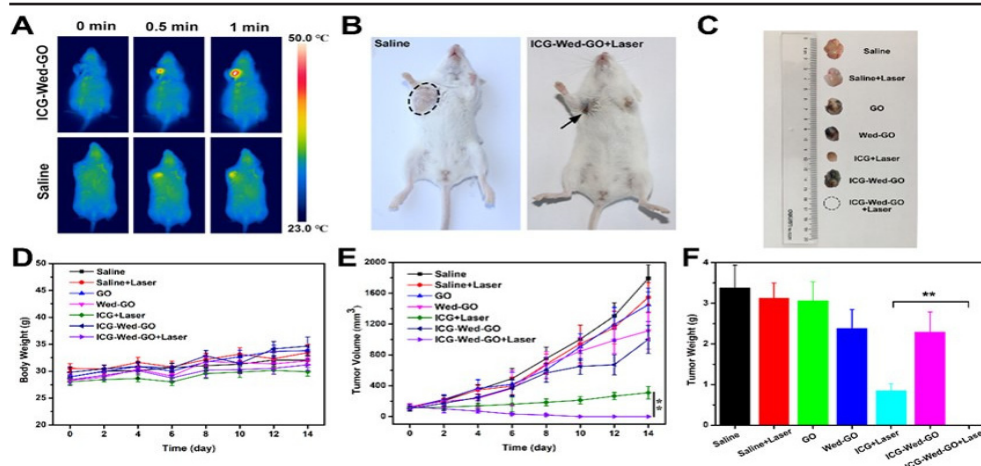
Figure 15: (A) Thermal images of U14 tumor-bearing mice exposed to NIR irradiation after injection of ICG-Wed-GO. **(B)** Photograph of tumor-bearing mice treated with ICG-Wed-GO and Saline under NIR irradiation on the 14th day. **(C)** Photograph of the tumors removed from the mice bearing U14 tumor after 14 day-post injection. **(D)** Body weight changes of tumor-bearing mice under different treatment. **(E)** Tumor volumes of tumor-bearing mice in different groups. **(F)** Tumor weights of mice in different groups after 14-day treatment [29].

References

1. Bray F, Ferlay J, Soerjomataram I, Siegel RL, Torre LA, et al. Global cancer statistics 2018: GLOBOCAN estimates of incidence and mortality worldwide for 36 cancers in 185 countries. CA: A cancer journal for clinicians. 2018; 68: 394-424.

2. Tran S, DeGiovanni PJ, Piel B, Rai P. Cancer nanomedicine: A review of recent success in drug delivery. Clinical and translational medicine. 2017; 6: 44.

3. Yun YH, Lee BK, Park K. Controlled drug delivery: Historical perspective for the next generation. Journal of Controlled Release. 2015; 219: 2-7.

4. Gregoriadis G, Swain CP, Wills EJ, Tavill AS. Drug-carrier potential of liposomes in cancer chemotherapy. The Lancet. 1974; 303: 1313-1316.

5. Ahn S, Seo E, Kim K, Lee SJ. Controlled cellular uptake and drug efficacy of nanotherapeutics. Scientific reports. 2013; 3: 1997.

6. Siegel RL, Miller KD, Jemal A. Cancer Statistics, 2017[J]. CA Cancer J Clin. 2017; 67: 7-30.

7. Zhao J, Koay EJ, Li T, Wen X, Li C. A hindsight reflection on the clinical studies of poly (I-glutamic acid)-paclitaxel. Wiley Interdisciplinary Reviews: Nanomedicine and Nanobiotechnology. 2018; 10: e1497.

8. Duncan R. Development of HPMA copolymer–anticancer conjugates: Clinical experience and lessons learnt. Advanced drug delivery reviews. 2009; 61: 1131-1148.

9. Yang J, Kopeček J. The light at the end of the tunnel-second generation HPMA conjugates for cancer treatment. Current opinion in colloid & interface science. 2017; 31: 30-42.

10. Sun Z, Xie H, Tang S, Yu XF, Guo Z, et al. Ultrasmall black phosphorus quantum dots: Synthesis and use as photothermal agents. Angewandte Chemie International Edition. 2015; 54: 11526-11530.

11. Yong Y, Cheng X, Bao T, Zu M, Yan L, et al. Tungsten sulfide quantum dots as multifunctional nanotheranostics for in vivo dual-modal image-guided photothermal/radiotherapy synergistic therapy. ACS nano. 2015; 9: 12451-12463.

12. Lv R, Yang P, Hu B, Xu J, Shang W, et al. In situ growth strategy to integrate up-conversion nanoparticles with ultrasmall CuS for photothermal theranostics. Acs Nano. 2017; 11: 1064-1072.

13. Li Z, Liu J, Hu Y, Howard KA, Li Z, et al. Multimodal imaging-guided antitumor photothermal therapy and drug delivery using bismuth selenide spherical sponge. ACS nano. 2016; 10: 9646-9658.

14. Espinosa A, Di Corato R, Kolosnjaj-Tabi J, Flaud P, Pellegrino T, et al. Duality of iron oxide nanoparticles in cancer therapy: Amplification of heating efficiency by magnetic hyperthermia and photothermal bimodal treatment. ACS nano. 2016; 10: 2436-2446.

15. Mo S, Chen X, Chen M, He C, Lu Y, et al. Two-dimensional antibacterial Pd@ Ag nanosheets with a synergetic effect of plasmonic heating and Ag+ release. Journal of Materials Chemistry B. 2015; 3: 6255-6260.

16. Sotiriou GA, Starsich F, Dasargyri A, Wurnig MC, Krumeich F, et al. Cancer Treatment: Photothermal Killing of Cancer Cells by the Controlled Plasmonic Coupling of Silica-Coated Au/Fe2O3 Nanoaggregates (Adv. Funct. Mater. 19/2014). Advanced Functional Materials. 2014; 24: 2817-2827.

17. Ma N, Jiang YW, Zhang X, Wu H, Myers JN, et al. Enhanced radiosensitization of gold nanospikes via hyperthermia in combined cancer radiation and photothermal therapy. ACS applied materials & interfaces. 2016; 8: 28480-28494.

18. Liu Z, Cheng L, Zhang L, Yang Z, Liu Z, et al. Sub-100 nm hollow Au-Ag alloy urchin-shaped nanostructure with ultrahigh density of nanotips for photothermal cancer therapy. Biomaterials. 2014; 35: 4099-4107.

19. Lyu Y, Fang Y, Miao Q, Zhen X, Ding D, et al. Intraparticle molecular orbital engineering of semiconducting polymer nanoparticles as amplified theranostics for in vivo photoacoustic imaging and photothermal therapy. ACS nano. 2016; 10: 4472-4481.

20. Luo S, Zhang E, Su Y, Cheng T, Shi C. A review of NIR dyes in cancer targeting and imaging. Biomaterials. 2011; 32: 7127-7138.

21. Tian Q, Jiang F, Zou R, Liu Q, Chen Z, et al. Hydrophilic Cu9S5 nanocrystals: A photothermal agent with a 25.7% heat conversion efficiency for photothermal ablation of cancer cells in vivo. ACS nano. 2011; 5: 9761-9771.

22. Zeng J, Zhang Q, Chen J, Xia Y. A comparison study of the catalytic properties of Au-based nanocages, nanoboxes, and nanoparticles. Nano letters. 2010 J; 10: 30-35.

23. Lin M, Wang D, Liu S, Huang T, Sun B, et al. Cupreous complex-loaded chitosan nanoparticles for photothermal therapy and chemotherapy of oral epithelial carcinoma. ACS applied materials & interfaces. 2015; 7: 20801-20812.

24. Feng Q, Zhang Y, Zhang W, Shan X, Yuan Y, et al. Tumor-targeted and multi-stimuli responsive drug delivery system for near-infrared light induced chemo-phototherapy and photoacoustic tomography. Acta biomaterialia. 2016; 38: 129-142.

25. Luo L, Bian Y, Liu Y, Zhang X, Wang M, et al. Combined near infrared photothermal therapy and chemotherapy using gold nanoshells coated liposomes to enhance antitumor effect. Small. 2016; 12: 4102.

26. He Y, Yang M, Zhao S, Cong C, Li X, et al. Regulatory mechanism of localized surface plasmon resonance based on gold nanoparticles-coated paclitaxel nanoliposomes and their antitumor efficacy. ACS Sustainable Chemistry & Engineering. 2018; 6: 13543-13550.

27. Cao W, He Y, Zhu R, He Y, Hao Z, et al. Nir light triggered size variable "remote-controlled cluster bomb" for deep penetration and tumor therapy. Chemical Engineering Journal. 2019; 375: 122080.

28. Bian K, Zhang X, Liu K, Yin T, Liu H, et al. Peptide-directed hierarchical mineralized silver nanocages for anti-tumor photothermal therapy. ACS Sustainable Chemistry & Engineering. 2018; 6: 7574-7588.

29. Zhang X, Luo L, Li L, He Y, Cao W, et al. Trimodal synergistic antitumor drug delivery system based on graphene oxide. Nanomedicine: Nanotechnology, Biology and Medicine. 2019; 15: 142-152.

30. Nikoobakht B, El-Sayed MA. Preparation and growth mechanism of gold Nanorods (NRs) using seed-mediated growth method. Chemistry of Materials. 2003; 15: 1957-1962.

31. Liu S, Pan J, Liu J, Ma Y, Qiu F, et al. Dynamically PEGylated and borate-coordination-polymer-coated polydopamine nanoparticles for synergetic tumor-targeted, chemo-photothermal combination therapy. Small. 2018; 14: 1703968.

32. Yan J, Yang L, Lin MF, Ma J, Lu X, et al. Polydopamine spheres as active templates for convenient synthesis of various nanostructures. Small. 2013; 9: 596-603.

33. Perrault SD, Walkey C, Jennings T, Fischer HC, Chan WC. Mediating tumor targeting efficiency of nanoparticles through design. Nano letters. 2009; 9: 1909-1915.

34. Wang J, Mao W, Lock LL, Tang J, Sui M, et al. The role of micelle size in tumor accumulation, penetration, and treatment. ACS nano. 2015; 9: 7195-7206.

35. Li HJ, Du JZ, Liu J, Du XJ, Shen S, et al. Smart superstructures with ultrahigh pH-sensitivity for targeting acidic tumor microenvironment: Instantaneous size switching and improved tumor penetration. ACS nano. 2016; 10: 6753-6761.

36. O'Neal DP, Hirsch LR, Halas NJ, Payne JD, West JL. Photo-thermal tumor ablation in mice using near infrared-absorbing nanoparticles. Cancer letters. 2004; 209: 171-176.

37. Liang C, Diao S, Wang C, Gong H, Liu T, et al. Tumor metastasis inhibition by imaging-guided photothermal therapy with single-walled carbon nanotubes. Advanced materials. 2014; 26: 5646.

38. Chen Z, Wang Q, Wang H, Zhang L, Song G, et al. Ultrathin PEGylated W18O49 Nanowires as a New 980 nm-Laser-Driven Photothermal Agent for Efficient Ablation of Cancer Cells In Vivo. Advanced materials. 2013; 25: 2095-2100.

39. Chen G, Jaskula-Sztul R, Esquibel CR, Lou I, Zheng Q, et al. Neuroendocrine Tumor-Targeted Upconversion Nanoparticle-Based Micelles for Simultaneous NIR-Controlled Combination Chemotherapy and Photodynamic Therapy, and Fluorescence Imaging. Advanced functional materials. 2017; 27: 1604671.

40. Bale SS, Asuri P, Karajanagi SS, Dordick JS, Kane RS. Protein-Directed Formation of Silver Nanoparticles on Carbon Nanotubes. Advanced materials. 2007; 19: 3167-3170.

41. Vijayaraghavan K, Nalini SK. Biotemplates in the green synthesis of silver nanoparticles. Biotechnology journal. 2010; 5: 1098-1110.

42. Wiley B, Sun Y, Xia Y. Synthesis of silver nanostructures with controlled shapes and properties. Accounts of Chemical Research. 2007; 40: 1067-1076.

43. Wang Z, Huang P, Jacobson O, Wang Z, Liu Y, et al. Biomineralization-inspired synthesis of copper sulfide–ferritin nanocages as cancer theranostics. ACS nano. 2016; 10: 3453-3460.

44. Schulz A, Wang H, van Rijn P, Böker A. Synthetic inorganic materials by mimicking biomineralization processes using native and non-native protein functions. Journal of Materials Chemistry. 2011; 21: 18903-18918.

45. Sóvágó I, Kállay C, Várnagy K. Peptides as complexing agents: Factors influencing the structure and thermodynamic stability of peptide complexes. Coordination Chemistry Reviews. 2012; 256: 2225-2233.

46. Patwardhan SV, Emami FS, Berry RJ, Jones SE, Naik RR, et al. Chemistry of aqueous silica nanoparticle surfaces and the mechanism of selective peptide adsorption. Journal of the American Chemical Society. 2012; 134: 6244-6256.

47. Liu Y, Goebl J, Yin Y. Templated synthesis of nanostructured materials. Chemical Society Reviews. 2013; 42: 2610-2653.

48. Li Y, Tang Z, Prasad PN, Knecht MR, Swihart MT. Peptide-mediated synthesis of gold nanoparticles: Effects of peptide sequence and nature of binding on physicochemical properties. Nanoscale. 2014; 6: 3165-3172.

49. Liang G, Ye D, Zhang X, Dong F, Chen H, et al. One-pot synthesis of Gd 3+-functionalized gold nanoclusters for dual model (fluorescence/magnetic resonance) imaging. Journal of Materials Chemistry B. 2013; 1: 3545-3552.

50. Guo C, Irudayaraj J. Fluorescent Ag clusters via a protein-directed approach as a Hg (II) ion sensor. Analytical chemistry. 2011; 83: 2883-2889.

51. Cui Y, Wang Y, Liu R, Sun Z, Wei Y, et al. Serial silver clusters biomineralized by one peptide. ACS nano. 2011; 5: 8684-8689.

52. Pazos E, Sleep E, Rubert Perez CM, Lee SS, Tantakitti F, et al. Nucleation and growth of ordered arrays of silver nanoparticles on peptide nanofibers: Hybrid nanostructures with antimicrobial properties. Journal of the American Chemical Society. 2016; 138: 5507-5510.

53. Wang Y, Cui Y, Zhao Y, Liu R, Sun Z, et al. Bifunctional peptides that precisely biomineralize Au clusters and specifically stain cell nuclei. Chemical Communications. 2012; 48: 871-873.

54. Song W, Wang Y, Liang RP, Zhang L, Qiu JD. Label-free fluorescence assay for protein kinase based on peptide biomineralized gold nanoclusters as signal sensing probe. Biosensors and Bioelectronics. 2015; 64: 234-240.

55. Xue W, Zhao X, Gao D, Gao F, Wang Z, et al. Octreotide acetate-templated self-assembly Pt nanoparticles and their anti-tumor efficacy. RSC Advances. 2015; 5: 42186-42192.

56. Wang Z, Xue W, Zhao X, Li Y, Liu Z, et al. Self-assembly of platinum nanochains using octreotide acetate template and their catalytic activity study. Materials Letters. 2016; 170: 160-162.

57. Zhang X, Yang C, Zhou J, Huo M. Somatostatin Receptor-Mediated Tumor-Targeting Nanocarriers Based on Octreotide-PEG Conjugated Nanographene Oxide for Combined Chemo and Photothermal Therapy. Small. 2016; 12: 3578-3590.

58. Lelle M, Kaloyanova S, Freidel C, Theodoropoulou M, Musheev M, et al. Octreotide-mediated tumor-targeted drug delivery via a cleavable doxorubicin-peptide conjugate. Molecular pharmaceutics. 2015; 12: 4290-4300.

59. Wang W, Lu W, Jiang L. AgCl and Ag/AgCl hollow spheres based on self-assemblies of a multi-amine head surfactant. Journal of colloid and interface science. 2009; 338: 270-275.

60. Shahzad A, Kim WS, Yu T. A facile synthesis of Ag/AgCl hybrid nanostructures with tunable morphologies and compositions as advanced visible light plasmonic photocatalysts. Dalton Transactions. 2016; 45: 9158-9165.

61. Sun W, Liu H, Hu J, Li J. Controllable synthesis and morphology-dependent photocatalytic performance of anatase TiO 2 nanoplates. Rsc Advances. 2015; 5: 513-520.

62. Zhang H, Fan X, Quan X, Chen S, Yu H. Graphene sheets grafted Ag@ AgCl hybrid with enhanced plasmonic photocatalytic activity under visible light. Environmental science & technology. 2011; 45: 5731-5736.

63. Sun Y. Controlled synthesis of colloidal silver nanoparticles in organic solutions: Empirical rules for nucleation engineering. Chemical Society Reviews. 2013; 42: 2497.

64. Wang Y, Chen P, Liu M. Synthesis of hollow silver nanostructures by a simple strategy. Nanotechnology. 2008; 19: 045607.

65. Jiang T, Song J, Zhang W, Wang H, Li X, et al. Au–Ag@ Au hollow nanostructure with enhanced chemical stability and improved photothermal transduction efficiency for cancer treatment. ACS applied materials & interfaces. 2015; 7: 21985-21994.

66. McGrath AJ, Chien YH, Cheong S, Herman DA, Watt J, et al. Gold over branched palladium nanostructures for photothermal cancer therapy. Acs Nano. 2015; 9: 12283-12291.

67. Jiang T, Song J, Zhang W, Wang H, Li X, et al. Au-Ag@ Au hollow nanostructure with enhanced chemical stability and improved photothermal transduction efficiency for cancer treatment. ACS applied materials & interfaces. 2015; 7: 21985-21994.

68. Liu Y, Ai K, Liu J, Deng M, He Y, et al. Dopamine-melanin colloidal nanospheres: An efficient near-infrared photothermal therapeutic agent for in vivo cancer therapy. Advanced materials. 2013; 25: 1353-1359.

69. Hsiao IL, Hsieh YK, Wang CF, Chen IC, Huang YJ. Trojan-horse mechanism in the cellular uptake of silver nanoparticles verified by direct intra-and extracellular silver speciation analysis. Environmental science & technology. 2015; 49: 3813-3821.

70. Jiang X, Miclăuş T, Wang L, Foldbjerg R, Sutherland DS, et al. Fast intracellular dissolution and persistent cellular uptake of silver nanoparticles in CHO-K1 cells: Implication for cytotoxicity. Nanotoxicology. 2015; 9: 181-189.

71. Pauksch L, Hartmann S, Rohnke M, Szalay G, Alt V, et al. Biocompatibility of silver nanoparticles and silver ions in primary human mesenchymal stem cells and osteoblasts. Acta biomaterialia. 2014; 10: 439-449.

72. Austin CA, Umbreit TH, Brown KM, Barber DS, Dair BJ, et al. Distribution of silver nanoparticles in pregnant mice and developing embryos. Nanotoxicology. 2012; 6: 912-922.

73. Cheng D, Xia H, Chan HS. Facile Fabrication of AgCl@ Polypyrrole– Chitosan Core– Shell Nanoparticles and Polymeric Hollow Nanospheres. Langmuir. 2004; 20: 9909-9912.

74. Bianco A. Graphene: Safe or toxic? The two faces of the medal. Angewandte Chemie International Edition. 2013; 52: 4986-4997.

75. Wang YW, Fu YY, Peng Q, Guo SS, Liu G, et al. Dye-enhanced graphene oxide for photothermal therapy and photoacoustic imaging. Journal of Materials Chemistry B. 2013; 1: 5762.

76. Johari P, Shenoy VB. Modulating optical properties of graphene oxide: Role of prominent functional groups. ACS nano. 2011; 5: 7640-7647.

77. Park S, Ruoff RS. Chemical methods for the production of graphenes. Nature nanotechnology. 2009; 4: 217.

78. Shim G, Kim MG, Park JY, Oh YK. Graphene-based nanosheets for delivery of chemotherapeutics and biological drugs. Advanced drug delivery reviews. 2016; 105: 205-227.

79. Hu D, Zhang J, Gao G, Sheng Z, Cui H, et al. Indocyanine green-loaded polydopamine-reduced graphene oxide nanocomposites with amplifying photoacoustic and photothermal effects for cancer theranostics. Theranostics. 2016; 6: 1043-1052.

80. Su S, Tian Y, Li Y, Ding Y, Ji T, et al. "Triple-punch" strategy for triple negative breast cancer therapy with minimized drug dosage and improved antitumor efficacy. ACS nano. 2015; 9: 1367-1378.

81. Wang Y, Xie Y, Li J, Peng ZH, Sheinin Y, et al. Tumor-penetrating nanoparticles for enhanced anticancer activity of combined photodynamic and hypoxia-activated therapy. ACS nano. 2017; 11: 2227-2238.

82. Liu Y, Yang F, Yuan C, Li M, Wang T, et al. Magnetic nanoliposomes as in situ microbubble bombers for multimodality image-guided cancer theranostics. ACS nano. 2017; 11: 1509-1519.

83. Zhang P, Hu C, Ran W, Meng J, Yin Q, et al. Recent progress in light-triggered nanotheranostics for cancer treatment. Theranostics. 2016; 6: 948-968.

84. Fan W, Yung B, Huang P, Chen X. Nanotechnology for multimodal synergistic cancer therapy. Chemical reviews. 2017; 117: 13566-13638.

85. Luo L, Bian Y, Liu Y, Zhang X, Wang M, et al. Combined near infrared photothermal therapy and chemotherapy using gold nanoshells coated liposomes to enhance antitumor effect. Small. 2016; 12: 4103-4112.

86. Wang Z, Chang Z, Lu M, Shao D, Yue J, et al. Janus silver/silica nanoplatforms for light-activated liver cancer chemo/photothermal therapy. ACS applied materials & interfaces. 2017; 9: 30306-30317.

87. Govindachari TR, Nagarajan K, Pai BR. 126. Chemical examination of Wedelia calendulacea. Part I. Structure of wedelolactone. Journal of the Chemical Society (Resumed). 1956: 629-632.

88. Benes P, Knopfova L, Trcka F, Nemajerova A, Pinheiro D, et al. Inhibition of topoisomerase IIα: Novel function of wedelolactone. Cancer letters. 2011; 303: 29-38.